DETECTION OF DEFECTS IN GROOVE TEXTURES OF HONED SURFACES

J. Beyerer and F. Puente León

Institut für Meß- und Regelungstechnik
Universität Karlsruhe (TH)
Postfach 6980
76128 Karlsruhe
Germany

Abstract - The automatic assessment of the texture of honed surfaces of cylinder bores based on microscopic grey level images is a demanding task. Although for some of the problems arising in this context, solutions are already given in literature [6,7,9], there remains a lot of work to be done due to the complexity of honing textures and the high quality demands made by combustion engine manufacturers. This paper deals with the special task of automatically detecting undesired defects like: folded metal, groove interrupts, smudgy groove edges etc. in honing textures. Therefore, two different image processing algorithms are presented. The first one searches for defects locally, whereas the second algorithm aims at detecting defective grooves in their entirety by exploiting the fact that, if a groove is affected, then usually several defects occur within the very same groove. The signal theory necessary to understand the algorithms is shortly presented. It is demonstrated that both approaches deliver reliable detection results for real honing textures.

1. INTRODUCTION

The surface quality of cylinder bores is essential for the operating characteristics of combustion engines. Especially oil consumption, running-in behaviour, noxious emissions and longevity depend highly on the quality of the microtexture, that is, on specific topographic features, which ensure good load bearing capabilities as well as good oil retention and flow properties. For grey iron, which is the most frequently used material for cylinder blocks, the working surface is finished by honing the bore. Characteristically, the resulting texture consists of two or more bands of parallel, stochastically placed grooves at different angles to the cylinder axis.

An approved method to investigate the microstructure of honed surfaces is to scan its topography with a stylus gauge (mechanically or optically) along a straight line. Alternatively, but less common, the surface can be inspected with a video camera equipped with a magnifying optical system. Both techniques are compared in Table 1.
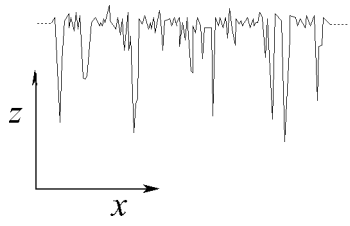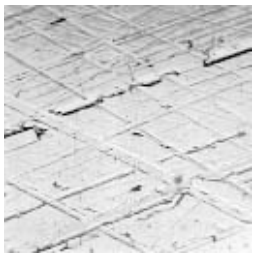
	Stylus gauge	**Grey level image**
	z ⌐ /\/\/\/\ → x	
Depth information	Yes	No
Lateral geometric (textural) information	No	Yes (Angle between grooves, courses of curved grooves, ...)
Dimension of measurement region	1	2
Covering the entire surface	Very lengthy	Possible with reasonable effort
Computational expense for data processing	Low	High
Non-contact measurement	Mechanical stylus: no Optical stylus: yes	Yes
Standardized parameters	Yes [1,2,3,4]	No
Distribution, industrial acceptance	High	Low

Table 1: Comparison between roughness traces from a stylus gauge and grey level images

Obviously, the data of both methods usefully complement each other in some ways. It would be desirable to scan the depth two-dimensionally to get a 3D-description [5] of the topography, because this would imply the depth information of the roughness trace as well as the textural (lateral geometric) information of the grey level image. Unfortunately, sensors which are able to acquire 3D-images in an acceptable time compared with the time necessary to take a grey level image are not available.

The scope of this paper is confined to the processing of grey level images of honed surfaces with the aim of detecting certain local defects. Up to now, texture quality of honed surfaces has been assessed by visual inspection of microscopic images by an expert. This approach is tedious and subjective; therefore it is desirable to develop methods allowing an automatic assessment of the honing texture.

One part of the quality information is related to the geometric and statistical properties of the groove texture, like crosshatch angle, balance of grooves and presence of plateaus. Methods following these criteria for the automatic assessment of honing textures can be found in [6,7]. Another part of the information relevant to surface quality is contained in the so-called background texture consisting of holes, cracks, flakes, material defects, graphite lamellae, material smearings, folded metal, groove interrupts, smudgy groove edges and foreign bodies.

In this paper we will focus on the automatic detection of objects and defects in the background texture. Special attention is paid to defects affecting grooves. On the one hand, these defects hinder the oil flow within the system of communicating canals established by the grooves, and on the other hand, they can be detected quite easily as deviations from ideal grooves. Fig. 1 shows the structure of the image processing schematically.

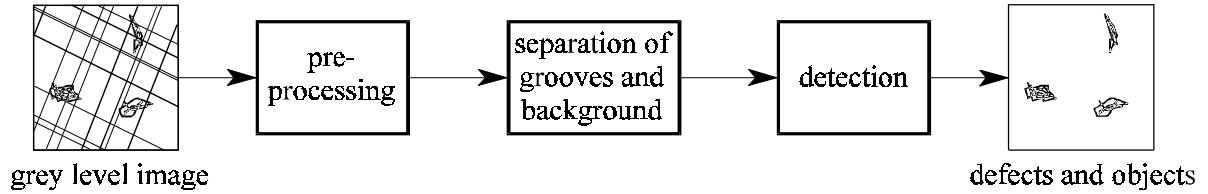
grey level image   defects and objects

Figure 1: Processing scheme

At first, texture inhomogeneities resulting from image acquisition (e.g. illumination inhomogeneities) as well as low frequency grey level fluctuations are eliminated to ease the following signal processing steps. The groove texture usually dominates the background texture, which contains the signal of interest. Therefore, grooves and background are splitted. This allows a separate access to both components in order to construct more reliable detection algorithms.

Section 2 deals with the signal theoretic description of honing textures and an algorithm for separating groove and background texture is addressed briefly. In subsection 3.1 an algorithm for local defect detection is presented, whereas in subsection 3.2 every groove as a whole is observed whether it is defective or not.

2. HONING TEXTURES AS TWO-DIMENSIONAL SIGNALS

The grey level images ridded of inhomogeneities are assumed to be realisations $s(\boldsymbol{x})$ of a zero-mean stationary random process. Where it is convenient, $s(\boldsymbol{x})$ is treated as a continuous signal of infinite extent. Of course, if some of the concepts shown in this paper are to be implemented on a computer, the consequences of spatial sampling and of restriction to a finite extent have to be taken into account [8].

It has been proven to be useful [6,7] to model the images as:

$$s(\boldsymbol{x}) = t(\boldsymbol{x}) + b(\boldsymbol{x}) \ . \tag{1}$$

$b(\boldsymbol{x})$ is the background texture. It is assumed to be zero-mean:

$$\mathrm{E}\{b(\boldsymbol{x})\} = 0 \ , \qquad \mathrm{E}\{\ \}: \text{expectation operator.} \tag{2}$$

$b(\boldsymbol{x})$ is isotropic, i.e. the autocorrelation function

$$\Phi_{bb}(\boldsymbol{\tau}) := \mathrm{E}\{b(\boldsymbol{x})b(\boldsymbol{x}+\boldsymbol{\tau})\} = f(\|\boldsymbol{\tau}\|) \ , \qquad \boldsymbol{\tau} = \left(\tau_x, \tau_y\right)^{\mathrm{T}} \tag{3}$$

3

is a function of $\|\tau\| = \sqrt{\tau_x^2 + \tau_y^2}$ only. The average power of $b(x)$ is $\sigma_b^2 = \Phi_{bb}(0)$ and the correlation length is τ_b.

Due to the stochastic nature of the cutting grain located on the honing tool the groove texture:

$$t(x) = \sum_{v=-\infty}^{\infty} g_v\left(x^T e_v - d_v\right) \tag{4}$$

is adopted to be a superposition of random straight grooves.

$g_v(\, . \,)$: random, independent identically distributed (i.i.d.) groove profiles.

$e_v = \left(\cos\alpha_v, \sin\alpha_v\right)^T$: normal vector of the v-th groove.

$\alpha_v \in [0, \pi)$: random, i.i.d. angles of the grooves. Ideally, they should be distributed according to the probability density function $p(\alpha_v) = \frac{1}{2}\delta(\alpha_v - \beta_1) + \frac{1}{2}\delta(\alpha_v - \beta_2)$, i.e. there should be two balanced bands of parallel grooves at the specific angles β_1 and β_2.

d_v : random, independent, uniformly distributed distances between the grooves and the spatial origin (see Fig. 2). The number q of distances falling into a randomly chosen interval of length L is Poisson distributed:

$$P(q) = e^{-\lambda L}\frac{(\lambda L)^q}{q!} \quad \text{with} \quad q = 0, \ldots, \infty \, , \quad \lambda: \text{spatial groove density}. \tag{5}$$

This is due to the fact that the grain locations on the tools are approximately a realisation of a two-dimensional Poisson point process.
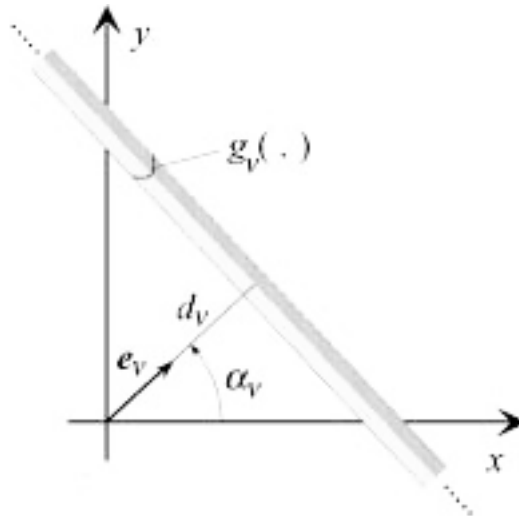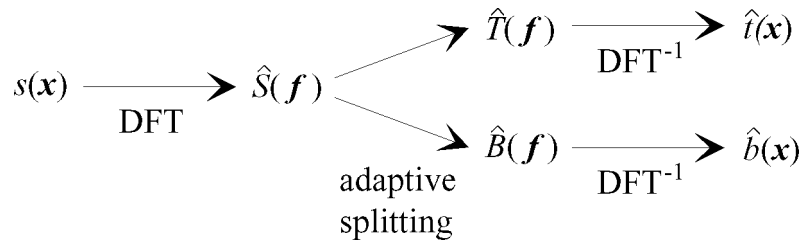

Figure 2: Signal model for the grooves

Based on the model (1), along with some small modifications, it is possible to synthesize artificial textures which look very similar to real honing textures [6,7]. This justifies the usage of this model in the development of signal processing algorithms for honed surfaces.

For grey level images $s(\boldsymbol{x})$ with the above-listed properties, a very effective and robust algorithm [9] exists to separate groove and background texture. The main idea is an adaptive (i.e. signal dependent) point-by-point splitting of the Discrete Fourier Transform (DFT) of $s(\boldsymbol{x})$ into two disjointed partial spectra, which are transformed back to the spatial domain to deliver estimates $\hat{t}(\boldsymbol{x})$ and $\hat{b}(\boldsymbol{x})$ for the textures $t(\boldsymbol{x})$ and $b(\boldsymbol{x})$ respectively (see Fig. 3).

$$s(\boldsymbol{x}) \xrightarrow{\text{DFT}} \hat{S}(\boldsymbol{f}) \begin{array}{c} \nearrow \hat{T}(\boldsymbol{f}) \xrightarrow{\text{DFT}^{-1}} \hat{t}(\boldsymbol{x}) \\ \searrow \hat{B}(\boldsymbol{f}) \xrightarrow{\text{DFT}^{-1}} \hat{b}(\boldsymbol{x}) \end{array}$$

adaptive splitting

$$\text{with } \hat{S}(\boldsymbol{f}) = \hat{T}(\boldsymbol{f}) + \hat{B}(\boldsymbol{f}) \text{ and } \text{supp}\{\hat{T}(\boldsymbol{f})\} \cap \text{supp}\{\hat{B}(\boldsymbol{f})\} = \varnothing$$

Figure 3: Separation of grooves and background

For the definition of both the continuous and the Discrete Fourier Transform see appendix 1. The DFTs are performed with a Fast Fourier Transform (FFT) algorithm [8].

The separation algorithm exploits the fact that the grooves are highly anisotropic in contrast to the perfect isotropy assumed for the background texture $b(\boldsymbol{x})$. A comprehensive discussion of the algorithm can be found in [9].

Fig. 4 shows a honed surface and the result of the separation. Note that the background texture contains all defects and objects, especially those affecting grooves.
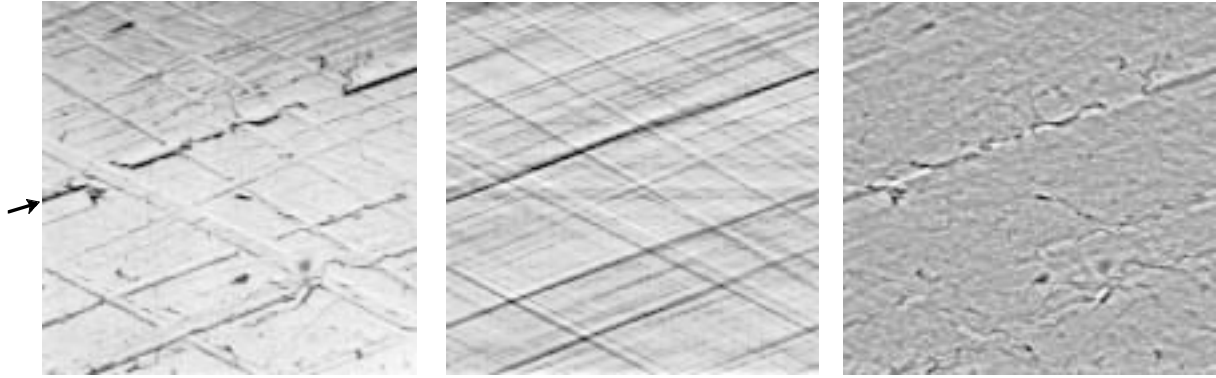
Fig. 4a: Honing texture[1]   Fig. 4b: Groove texture   Fig. 4c: Background texture

It should be emphasized that an accurate separation of groove and background texture is a fundamental preprocessing step for a reliable detection of defects in textures of honed surfaces.

3.   DETECTION OF DEFECTS

In the former section, the results of the separation algorithm were presented. Now we will focus on the obtained background texture, which contains the main information concerning defects and objects. In this section we will discuss two different approaches that will allow a detection of defects based on the background image: local and global detection.

In the local detection algorithms the decision whether a small area is defective is taken point-by-point. However, when defects are present in honed surfaces, they use to extend along grooves. That is, the locations of defects are not absolutely random, rather if they appear they are concentrated along straight lines (see Fig. 4a). Therefore, in the global detection approach, the decision whether a defect is present is taken globally for each groove. This way the detection reliability can be significantly improved.

3.1   *Local Detection of Defects*

This section is concerned with a general approach to local detection of defects. More precisely, a processing scheme will be presented that will allow to perform a segmentation of the background image in two different region types: defects and non-defective areas.

---

[1]The grey level images throughout this paper are digitized with $N{\times}N{=}256{\times}256$ pixels and with 8 bit grey values.

6

3.1.1   *General Structure*

The general structure of the local detection algorithms is shown in Fig. 5. The input image is the background texture $\hat{b}(\boldsymbol{x})$.

Figure 5: General structure of the local detection algorithms

The defect enhancement represents the most important step in the segmentation procedure. By means of adequate signal processing methods, defects can be enhanced while homogeneous regions do not generate any significant response. Spot and edge detectors have proven to be well suited for this purpose.

The following binarization compares the result of the defect enhancement with a threshold. This leads to a segmentation into defective and non-defective areas.

The aim of the post-processing step is to eliminate small defective regions whose area is smaller than a minimum size. Such small areas would not be treated as defects when being examined by an expert because they are not visually conspicuous and they can also arise as artifacts due to the processing of noise.

3.1.2   *An Example of Local Detection*

As an example of local detection, an algorithm based on a well-known linear edge detection operator, the Laplacian-of-Gaussian (LoG), is presented. This operator is based on the idea of using the zero-crossings in the second directional derivative to detect intensity changes. The differentiation process causes an amplification of high spatial frequencies. Therefore smoothing by a low-pass filter has to be performed simultaneously. Based on analytical considerations, Marr and Hildreth proposed the use of a Gaussian smoothing filter [10].

The impulse response of the LoG-Filter is given by the second derivative of a two-dimensional Gaussian density $G(\boldsymbol{x})$:

$$l(\boldsymbol{x}) = -\Delta G(\boldsymbol{x}) = \frac{2\sigma^2 - \|\boldsymbol{x}\|^2}{2\pi\sigma^6} e^{-\frac{\|\boldsymbol{x}\|^2}{2\sigma^2}} \ , \qquad \Delta := \frac{\partial^2}{\partial x^2} + \frac{\partial^2}{\partial y^2} \tag{6}$$

In the first step of the presented algorithm, a convolution with the LoG-filter is performed:

$$k(\boldsymbol{x}) := \hat{b}(\boldsymbol{x}) ** l(\boldsymbol{x}) = \int\limits_{-\infty}^{\infty} \int\limits_{-\infty}^{\infty} \hat{b}(\boldsymbol{v}) l(\boldsymbol{x} - \boldsymbol{v}) d\boldsymbol{v} \tag{7}$$

This operator yields zero-crossings at locations where edges are present. By means of a further processing step irrelevant contours are to be suppressed while those which actually stand for defects are to be retained.

7

Due to the band-pass character of this filter, high spatial frequencies are suppressed. Thus grey level changes are smoothed. The elimination of low frequencies transforms the large grey level changes of defects as well as small level fluctuations remaining after the Gaussian smoothing into zero-crossings. In order to suppress contours not corresponding with edges of defects, contour candidates are weighted with their zero-crossing slope. This leads to a gradient-like image $\zeta(\boldsymbol{x})$ which is zero except for the locations of the zero-crossings of $k(\boldsymbol{x})$.

$$\zeta(\boldsymbol{x}) := \begin{cases} \|\nabla k(\boldsymbol{x})\| & \text{if } k(\boldsymbol{x}) = 0 \\ 0 & \text{otherwise} \end{cases} \tag{8}$$

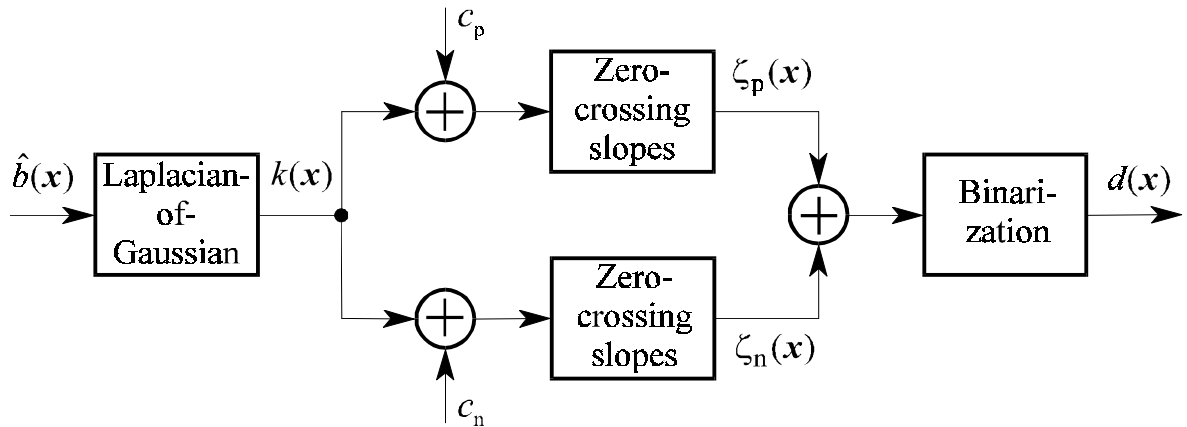Fig. 6 shows the block diagram of the algorithm based on the LoG-Filter.

Figure 6: Structure of the LoG-Algorithm

There is still one important drawback of the LoG-filter that has to be discussed. If the LoG-filter mask is much greater than the grey level plateaus between the edges, the zero-crossings will be displaced relative to the locations of the true edges. For example, if an LoG-filtering with a mask of width $w = 35$ is applied to defects of a typical extension of $a = 4$ pixels, straight contours will be shifted by $(w - a) / 2 = 15.5$ pixels [11]. On the other side, much smaller filter masks would lead to poor results because of the noise sensitivity of the Laplace operator. An improvement of the detection reliability is achieved at the expense of an increasing uncertainty regarding the location of contours.

However, there is an alternative in order to improve the contour localization despite of the strong smoothing. For this purpose, it has to be distinguished between the detection of light and dark defective patterns. If light patterns have to be detected, we may add a negative offset c_n to the filtered image before we search for zero-crossings. This way the undesired displacement of the contours can be partially compensated. In order to detect dark patterns, we may proceed in an analogue way, but adding a positive offset c_p this time. For more information on this topic see [11].

Fig. 7b shows the slope of the zero-crossings $\zeta_p(\boldsymbol{x})$ of Fig. 7a after having added a positive offset c_p to $k(\boldsymbol{x})$. Note that all contours extracted by means of the locations of zero-crossings of $k(\boldsymbol{x}) + c, \forall c \in \mathbf{R}$ are closed.
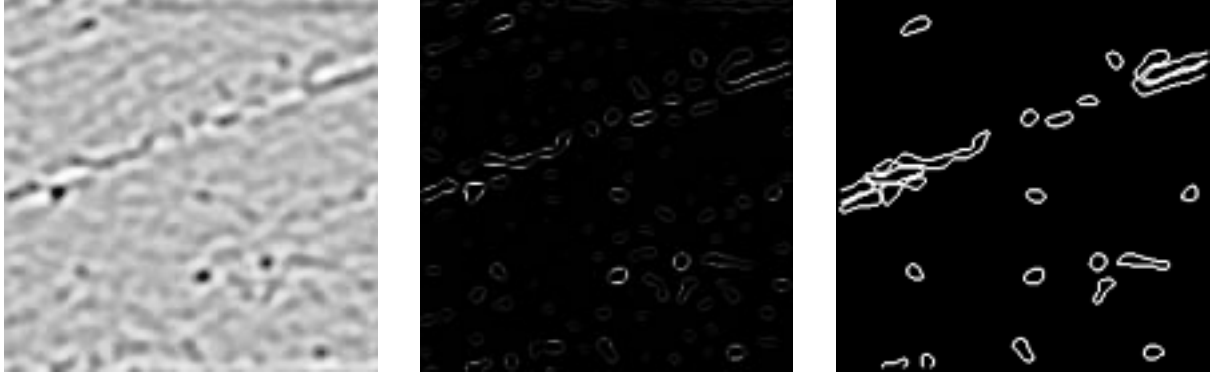

Fig. 7a: LoG-Filtering   Fig. 7b: Zero-crossing slopes   Fig. 7c: Binary result

In the next step the contours have to be classified as those which denote defects and those which can be assigned to the slight grey level changes of the background. It is convenient not to take this decision point-by-point, but only once for each closed contour. For this purpose the average slope along the contour is compared with a threshold. Fig. 7c shows the result of the contour classification. Most of the detected contours correspond with the defects of interest, especially with those along the groove labeled with an arrow in Fig. 4a.

3.2 *Global Detection of Defects*

In this section an algorithm that allows a global detection of defective grooves is presented. In order to facilitate the comprehension of its method, an simpler algorithm for detecting grooves will be described first. Following this, the algorithm will be expanded so that only defective grooves will be detected.

3.2.1 *Radon Transform*

The Radon Transform is mainly known from computer tomography and is defined as [12]:

$$\mathrm{R}\{s(\boldsymbol{x})\} = \breve{s}(\varphi, u) := \int\limits_{-\infty}^{\infty} \int\limits_{-\infty}^{\infty} s(\boldsymbol{x}) \delta(\boldsymbol{x}^{\mathrm{T}} \boldsymbol{e}_\varphi - u)\, dx\, dy \tag{9}$$

The transformation kernel consists of δ-lines with normal vector $\boldsymbol{e}_\varphi = (\cos\varphi, \sin\varphi)^{\mathrm{T}}$, $\varphi \in [0, \pi)$ and a signed offset u to the origin. The Radon Transform represents the set of all parallel projections of the signal $s(\boldsymbol{x})$. The relation between an image and its Radon Transform is illustrated in Fig. 8. In appendix 2 an efficient way to perform the Radon Transform of an image is described.
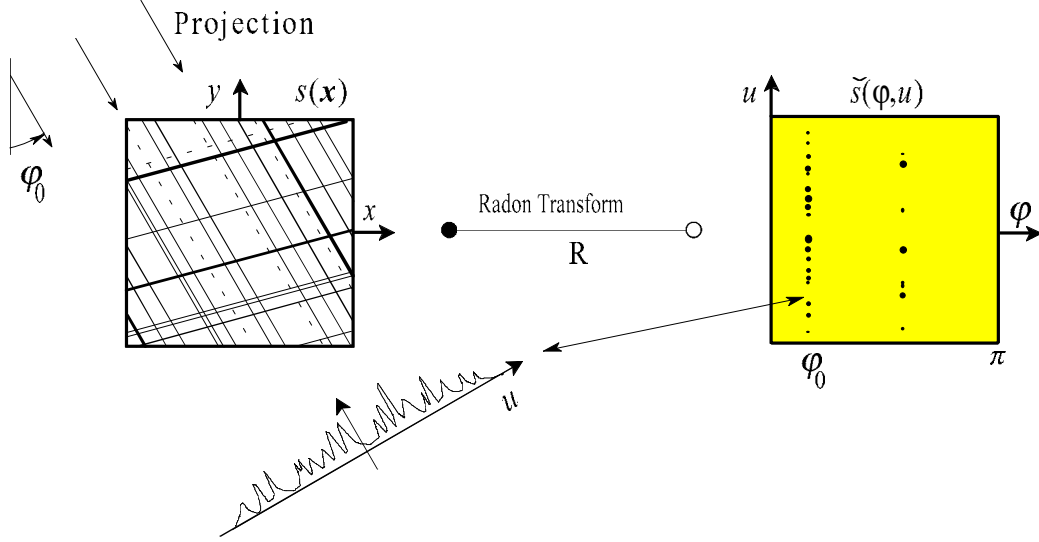
Figure 8: Illustration of the Radon Transform

The Radon Transform is a tool particularly suited to analyze straight structures in grey level images. Since the transformation kernel is a parametrized δ-line, straight structures like grooves are concentrated onto distinct peaks of $\breve{s}(\varphi,u)$. Isotropic structures however, are smeared all over the φ,u-domain. The background texture $b(\boldsymbol{x})$ is modeled as an isotropic stationary random process with an average power σ_b^2 and a correlation length of τ_b. The SNR_1 (Signal-to-Noise-Ratio) in the x,y-domain for the grooves $g_v(\,.\,)$ as the signals of interest and for $b(\boldsymbol{x})$ regarded as noise is:

$$\text{SNR}_1 = \frac{\max_\xi\{g_v(\xi)\}^2}{\sigma_b^2} \quad .\tag{10}$$

The SNR_2 of the corresponding Radon Transform results in:

$$\text{SNR}_2 \approx \frac{\max_\xi\{g_v(\xi)\}^2 L^2(\varphi,u)}{\sigma_b^2 L(\varphi,u)\tau_b} \quad ,\tag{11}$$

$$L(\varphi,u) = \text{R}\left\{\text{rect}\left(\tfrac{x}{N\Delta x}\right)\text{rect}\left(\tfrac{y}{N\Delta y}\right)\right\}, \qquad \text{rect}\left(\tfrac{\kappa}{K}\right) := \begin{cases} 1 & \text{for} & |\kappa| \leq \tfrac{1}{2}K \\ 0 & & \text{otherwise} \end{cases}.\tag{12}$$

$L(\varphi,u)$ is the length of the intersection of the δ-line $\delta\left(\boldsymbol{x}^{\text{T}}\boldsymbol{e}_\varphi - u\right)$ and the $N \times N$-aperture of the image. The ratio of the two SNRs:

$$\frac{\text{SNR}_2}{\text{SNR}_1} \approx \frac{L(\varphi,u)}{\tau_b}\tag{13}$$

shows that if $L(\varphi,u) \gg \tau_b$, grooves are strongly enhanced after Radon Transform.

It should be mentioned that the Hough Transform, which is a well-known tool for line detection in digital image processing, is a binary version of the Radon Transform [12].

10

3.2.2 *Detection of Grooves*

The basic idea of the groove detection algorithm consists in observing a pattern integrally along every straight line in the image plane. To perform the integration we make use of the Radon Transform.

Pronounced grooves of honed surfaces show clearly darker grey levels than the background (see Fig. 4a). When performing an integration of the grey level function along grooves, we expect to obtain negative peaks in the Radon plane. On the other hand, an integration across the groove texture will yield, on the average, vanishing values because the local mean of $\hat{t}(\boldsymbol{x})$ is zero (see Fig. 8).

In the schematic representation in Fig. 8 a problem can be already recognized: the minima we obtain for each groove do not depend only on the amplitude of each groove in the space domain but also on their location relative to the image aperture. The reason is that the length of the lines we integrate along, depends on the parameters φ and u. Therefore, the Radon transformed image is divided by the projection length $L(\varphi,u)$ to homogenize the peak heights [13]. Fig. 9a shows the result for Fig. 4b as input image. The dark peaks in the Radon plane correspond with grooves in the spatial domain.
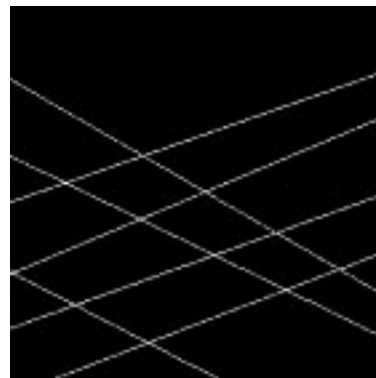

Fig. 9a: Radon Transform/$L(\varphi,u)$ Fig. 9b: Binary result

By further processing of Fig. 9a, the most significant grooves can be detected [13,15]. The binary result of the detection corresponds with the grooves shown in Fig. 9b.

3.2.3 *Global Defect Detection Algorithm*

In this section we are interested in detecting defective grooves in their entirety. For this purpose, we want to exploit the fact, that if a groove is defective at all, then usually several defects occur within the very same groove. As a consequence, the grey levels of the background image $\hat{b}(\boldsymbol{x})$ show large variances along the courses of the defective grooves. To measure these variances, $\hat{b}(\boldsymbol{x})$, which is locally zero-mean due to the suppression of low frequency components in the preprocessing step in Fig. 1, is squared (see Fig. 10a) and integrated along straigth lines. Once again, this integration is done by a Radon Transform. Thus, the collinearly arranged defects of a typical

defective groove result in a pronounced maximum in the Radon domain at the coordinates α_v, d_v , which describe the course of the groove (see Fig. 2 and 10b).
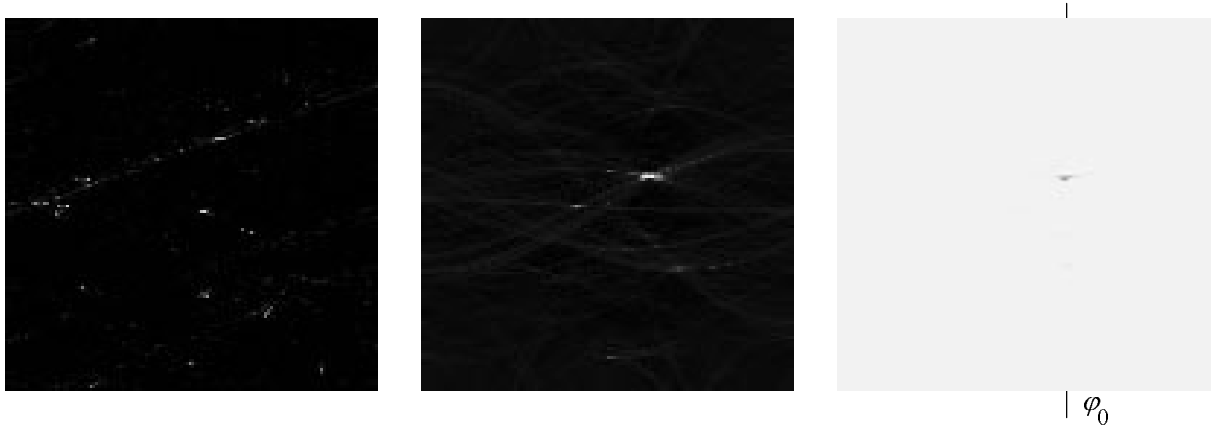

Fig. 10a: Squared image $\hat{b}^2(\boldsymbol{x})$

Fig. 10b: Radon Transform of Fig. 10a

Fig. 10c: Multiplication of Fig. 9a and Fig. 10b

The Radon Transform domain allows an integral analysis of collinear defects. In the Radon domain pronounced peaks appear at the coordinates of all grooves containing many defects (see Fig. 10b). All these peaks can be detected more easily and more reliably in the Radon domain.
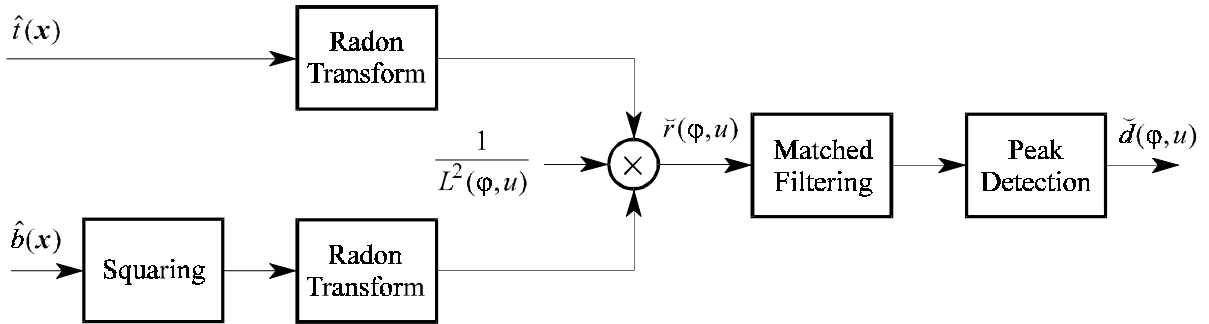

Figure 11: Structure of the algorithm for global detection of defects

In order to avoid a further consideration of more than two maxima of $\hat{b}^2(\boldsymbol{x})$, if they do not belong to the same groove or to a groove at all, $\mathrm{R}\{\hat{t}(\boldsymbol{x})\}$ and $\mathrm{R}\{\hat{b}^2(\boldsymbol{x})\}$ are combined multiplicatively (see Fig. 11).

The influence of the image aperture is compensated by dividing each Radon Transform by the projection length function $L(\varphi, u)$.

All in all, only grooves having a sufficiently high amplitude in $\hat{t}(\boldsymbol{x})$ as well as a sufficiently high variance along their courses in $\hat{b}(\boldsymbol{x})$ result in extrema after multiplying both input branches of Fig. 11. If we compare Fig. 10c with Fig. 10b, we can immediately recognize the enhancement that can be achieved by incorporating knowledge about the groove locations.

The effect of the combination becomes particularly clear if we transform the image Fig. 10c back into the spatial domain. In Fig. 12a the inverse Radon Transform of the multiplicatively combined signals is shown. Except for small disturbances, only defective grooves can be seen in this image.

Fig. 12a: Inverse Radon transform of Fig. 10c

Fig. 12b: Radon domain after matched filtering

Fig. 12c: Binary result

A further enhancement of the relevant information can be achieved with a matched filter. It performs a correlation with the expected shape $c(\varphi,u)$ of the extrema contained in $\breve{r}(\varphi,u)$.

$$\breve{r}(\varphi,u)\otimes\otimes c(\varphi,u)=\int\limits_{0}^{\pi}\int\limits_{-\infty}^{\infty}\breve{r}(\alpha,v)c(\varphi+\alpha,u+v)\,dv\,d\alpha \tag{14}$$

Such a filter is optimal for detecting a known signal in a background of white additive noise. However, in this case the noise in the Radon domain resulting from the background texture $\hat{b}(x)$ is not white and therefore the matched filter only represents a sub-optimal solution.

In order to perform the matched filtering, the shape of the signal we want to detect has to be given. A thorough analysis of $\breve{r}(\varphi,u)$ shows, that a separable filter kernel $c(\varphi,u)=c_1(\varphi)c_2(u)$ works quite well, if $c_2(u)$ is chosen to be a piecewise linear approximation of the peaks in Fig. 13 and $c_1(\varphi)$ is chosen to be a one-dimensional binomial filter [14]. The separability allows to do the filtering with two consecutive one-dimensional correlations. Fig. 12b shows the result of the matched filtering.
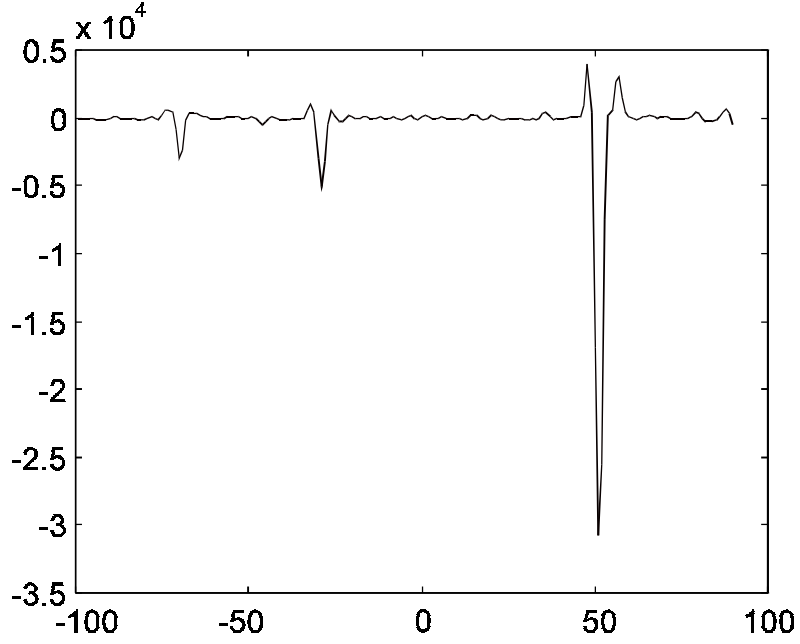
Figure 13: Trace in *u*-direction through the multiplicatively combined Radon plane Fig. 10c at $\varphi = \varphi_0$

After the matched-filtering the resulting image shows distinct peaks at locations at which a similarity between the Radon domain and the groove pattern $c(\varphi,u)$ exists. In order to avoid the detection of small peaks as the result of disturbances, the detection of maxima is combined with a threshold. Only local maxima exceeding a given threshold are extracted.

It is desirable to derive an adequate threshold γ from the filtered signal in the Radon domain. For this purpose an adaptive threshold based on the average m and the standard deviation s of the result obtained by matched filtering was proposed in [13]:

$$\gamma = m + k \cdot s \tag{15}$$

We chose the parameter value $k = 7$. The peaks detected by means of this rule from the filtered image Fig. 12b correspond with the grooves represented in Fig. 12c. It can be clearly seen that these are the most salient defective grooves in the original image Fig. 4a.

4   DISCUSSION

Both image processing algorithms presented in this paper are reliable tools in order to detect defects in honing textures. But their respective objectives are slightly different.

The global detection method aims at detecting defective grooves as a whole. Therefore, defects outside the grooves are ignored. Moreover, the final result (see Fig. 12c) contains no detailed information about location, form, and number of defects within a groove considered to be defective. However, since the global

14

detection averages all information available about a groove, the method behaves quite robustly.

The local detection method searches for defects within grooves as well as for those lying outside. Additionally, detailed information about location, form, and number of defects is available (see Fig. 7c). On the other hand, if global statements are required, the defects could be evaluated statistically to condense the local information into a few descriptors. Here, the knowledge about groove locations (see 3.2.2) could be considered as well.

Which of both methods should be preferred depends on the concrete aims of the image analysis.

5   CONCLUSIONS

Two reliable image processing algorithms have been presented for the automatic detection of undesired defects in honing textures of cylinder bores. The first one searches for defects locally, whereas the second one works globally in the sense that grooves, which are heavily affected with defects, are detected in their entirety. The good performance of both algorithms has been demonstrated with real honing textures.

The presented methods are important contributions towards an automatic quality assessment of honed surfaces of cylinder bores. Both algorithms can be carried out on signal processing hardware within the process cycle-time, which is about 30 to 60 seconds. On the other hand, there are also automatic measurement devices for cylinder bores available that acquire microscopic video images of the honing texture as well as some other surface data within a production line for cylinder blocks. A future aim will be to equip such a device with signal processing software in order to assess the quality of honed surfaces automatically.

ACKNOWLEDGEMENTS

REFERENCES

[1]   DIN 4760: *Gestaltsabweichungen: Begriffe, Ordnungssystem* (1982).

[2]   DIN 4762: *Oberflächenrauheit: Begriffe, Oberfläche und ihre Kenngrößen* (1989).

[3]   DIN 4768: *Ermittlung der Rauheitsmeßgrößen R_a, R_z, R_{max} mit elektrischen Tastschnittgeräten,* Blatt 1: Grundlagen (1974).

[4]   DIN 4776: *Rauheitsmessung: Kenngrößen R_k, R_{pk}, R_{vk}, M_{r1}, M_{r2} zur Beschreibung des Materialanteils im Rauheitsprofil*, Entwurf (1985).

[5]   K. J. STOUT, P. J. SULLIVAN et al.: *The Development of Methods for the Characterisation of Roughness in Three Dimensions*, University of Birmingham, Edgbaston (1993).

[6]   J. BEYERER, *Model based Analysis of Groove Textures*, IMEKO TC1 and TC7 Colloquium: State and Advances of Measurement and Instrumentation Science, London, 360-369 (1993).

[7]   J. BEYERER, *Analyse von Riefentexturen*, VDI Verlag, Düsseldorf (1994).

[8]   E. O. BRIGHAM, *The Fast Fourier Transform and its Applications*, Prentice Hall, Englewood Cliffs, New Jersey (1988).

[9]   J. BEYERER, *Suppression of stochastically placed, straight toolmarks to enhance objects and defects*, Technisches Messen 59, Nr. 10, 389-397 (1992).

[10]   D. MARR and E. HILDRETH, *Theory of edge detection*, Proceedings of the Royal Society London B-207, 187-217 (1980).

[11]   A. HUERTAS and G. MEDIONI, *Detection of Intensity Changes with Subpixel Accuracy Using Laplacian-Gaussian Masks*, IEEE Trans. on PAMI, Vol. 8, No. 5, 651-664 (1986).

[12]   S. R. DEANS, *The Radon Transform and Some of its Applications.* John Wiley & Sons, New York (1983).

[13]   H. FUHRMANN, *Riefendetektion und Schätzung der Lageparameter von Riefen in Grauwertbildern spanend bearbeiteter Oberflächen*, Master thesis at the Institut für Meß- und Regelungstechnik, Universität Karlsruhe (TH) (1993).

[14]   B. JÄHNE, *Digitale Bildverarbeitung*, Springer, Berlin (1991).

[15]   F. PUENTE LEÓN, *Lokale Detektion von Defekten an Riefen gehonter Kolbenlaufbahnen*, Master thesis at the Institut für Meß- und Regelungstechnik, Universität Karlsruhe (TH) (1994).

[16]   R. BAMLER, *Mehrdimensionale lineare Systeme, Fourier-Transformation und δ-Funktionen*, Springer, Berlin (1989).

[17]   W. K. PRATT, *Digital Image Processing*, John Wiley & Sons, New York (1991).

APPENDIX 1: CONTINUOUS AND DISCRETE FOURIER TRANSFORM

Continuous Fourier Transform:

$$S(\boldsymbol{f}):= \int_{-\infty}^{\infty}\int_{-\infty}^{\infty} s(\boldsymbol{x})e^{-j2\pi \boldsymbol{f}^{\mathrm{T}}\boldsymbol{x}}\,d\boldsymbol{x} \qquad s(\boldsymbol{x}) = \int_{-\infty}^{\infty}\int_{-\infty}^{\infty} S(\boldsymbol{f})e^{j2\pi \boldsymbol{f}^{\mathrm{T}}\boldsymbol{x}}\,d\boldsymbol{f}$$

Discrete Fourier Transform (DFT):

Without loss of generality, the supports of the discrete signals in the spatial ($\to \Omega_{\boldsymbol{x}}$) and frequency domains ($\to \Omega_f$) are fixed to be quadratic with an edge length of N pixels, centered around the origins of the respective domain.

$$\hat{S}(\boldsymbol{f}) = \hat{S}\!\left(\tfrac{k}{N\Delta x}, \tfrac{l}{N\Delta y}\right) = \Delta x \Delta y \sum_{(m,n)\in\Omega_{\boldsymbol{x}}} s(\boldsymbol{x})e^{-j2\pi\frac{km+ln}{N}}$$

$$s(\boldsymbol{x}) = s(n\Delta x,\, m\Delta y) = \left(N^{2}\Delta x\Delta y\right)^{-1} \sum_{(k,l)\in\Omega_f} \hat{S}(\boldsymbol{f})e^{j2\pi\frac{km+ln}{N}}$$

Position vector: $\quad \boldsymbol{x} = \underbrace{\begin{pmatrix} x \\ y \end{pmatrix}}_{\text{continuous case}} = \underbrace{\begin{pmatrix} m\Delta x \\ n\Delta y \end{pmatrix}}_{\text{discrete case}}$

Frequency vector: $\quad \boldsymbol{f} = \underbrace{\left(f_x, f_y\right)^{\mathrm{T}}}_{\text{continuous case}} = \underbrace{\left(\tfrac{k}{N\Delta x},\ \tfrac{l}{N\Delta y}\right)^{\mathrm{T}}}_{\text{discrete case}}$

Note that $s(m\Delta x,\, n\Delta y)$ are samples of the continuous signal $s(\boldsymbol{x})$ but that the DFT $\hat{S}\!\left(\tfrac{k}{N\Delta x}, \tfrac{l}{N\Delta y}\right)$ is generally only an approximation of the samples $S\!\left(\tfrac{k}{N\Delta x}, \tfrac{l}{N\Delta y}\right)$ of the Fourier Transform $S(\boldsymbol{f})$.

APPENDIX 2: THE PROJECTION SLICE THEOREM

The Projection Slice Theorem connects the two-dimensional Fourier Transform with the Radon Transform. It states that the parallel projection of a signal $s(\boldsymbol{x})$ is equal to the inverse one-dimensional Fourier Transform of a central slice of $S(\boldsymbol{f})$ perpendicular to the direction of projection (see Fig. 14).
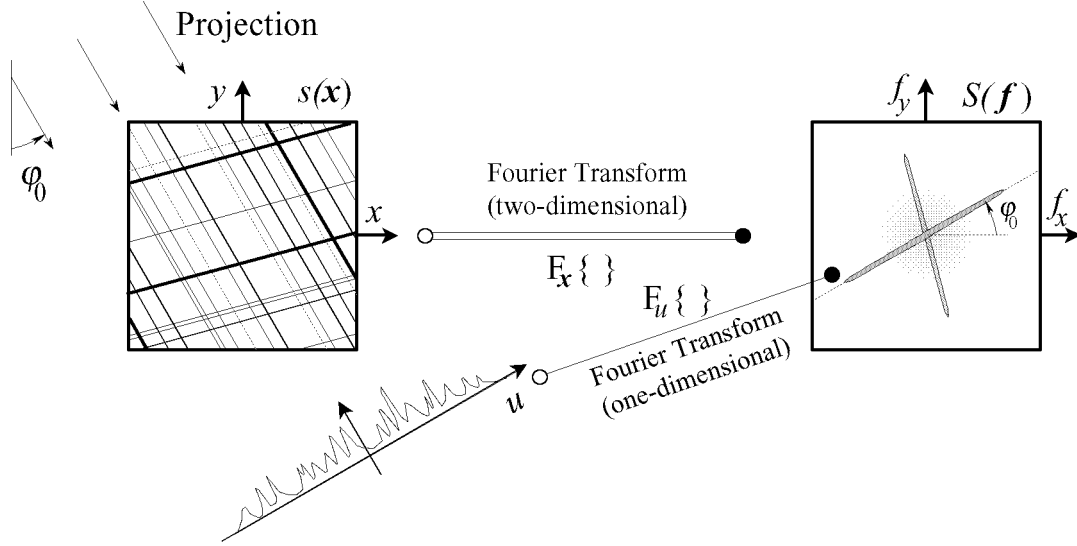
Figure 14: The Projection Slice Theorem

Formally, the Projection Slice Theorem can be written as:

$$\mathrm{F}_u\{\breve{s}(\varphi,u)\} = \int_{-\infty}^{\infty} \breve{s}(\varphi,u)e^{-j2\pi f_u u}\,du = \left[\int_{-\infty}^{\infty}\int_{-\infty}^{\infty} s(\pmb{x})e^{-j2\pi \pmb{f}^{\mathrm{T}}\pmb{x}}\,d\pmb{x}\right]_{\pmb{f}=f_u \pmb{e}_\varphi} = S\!\left(f_u \pmb{e}_\varphi\right) \quad (16)$$

A proof of the Projection Slice Theorem can be found in [12] or [16]. The theorem allows to implement the Radon Transform efficiently by means of the Fast Fourier Transform (FFT), which is a fast algorithm for the DFT [8]. Therefore, the DFT of $s(\pmb{x})$ is resampled on a polar grid with the coordinates f_u and φ. Since the discrete points of the rectangular and the polar coordinate system do not coincide generally, the values of $\mathrm{DFT}_{2D}\{s(\pmb{x})\}$ have to be interpolated.

$$\breve{s}(\varphi,u) \approx \mathrm{DFT}_{1D}^{-1} \Big\{ \underset{rect\to polar}{\mathrm{Bilin}} \big\{\mathrm{DFT}_{2D}\{s(\pmb{x})\}(f_u\cos\varphi, f_u\sin\varphi)\big\}\Big\} \quad (17)$$

We have found that this can be accomplished satisfactorily by bilinear interpolation (Operator: Bilin{ }) [17]. At last, each slice is mapped with an one-dimensional DFT^{-1} into the Radon domain.

To implement eq. (17) on a computer the space and frequency variables are discretized as:

$$u = n_u \Delta u \qquad\qquad n_u = -\frac{N_u}{2}+1,\dots\dots,\frac{N_u}{2}$$

$$\varphi = n_\varphi \Delta\varphi = \begin{cases} \angle f & \text{for } \angle f \in [0,\pi) \\ \angle f - \pi & \text{for } \angle f \in [\pi,2\pi) \end{cases} \qquad n_\varphi = 0,\dots\dots,N_\varphi - 1$$

$$f_u = n_{f_u}\Delta f_u = \begin{cases} \|\pmb{f}\| & \text{for } \angle f \in [0,\pi) \\ -\|\pmb{f}\| & \text{for } \angle f \in [\pi,2\pi) \end{cases} \qquad n_{f_u} = -\frac{N_{f_u}}{2}+1,\dots\dots,N_{f_u}$$

18

Eq. (17) is a discrete approximation of the continuous Radon Transform. The accompanying error will be small, if the Sampling Theorem of Computer Tomography:

$$N_\varphi > \frac{N\pi}{q\sqrt{2}}$$

(18)

is fulfilled [16]. q is the oversampling factor of the discrete image $s(\boldsymbol{x})$. For $q \approx 1.2$ (typical for the images used in this paper) and $N = 256$, N_φ should be greater than 474. Within this work, $N_\varphi = N_u = N_{f_u} = 512$ was chosen.